Visible Spectroscopy of the Polana-Eulalia Family Complex: Spectral Homogeneity

J. de León[a,b], N. Pinilla-Alonso[c], M. Delbó[d], H. Campins[e], A. Cabrera-Lavers[f,a], P. Tanga[d], A. Cellino[g], P. Bendjoya[d], J. Licandro[a,b], V. Lorenzi[h], D. Morate[a,b], K. Walsh[i], F. DeMeo[j], Z. Landsman[e]

[a]*Instituto de Astrofísica de Canarias, C/Vía Láctea s/n, 38205, La Laguna, Spain*
[b]*Department of Astrophysics, University of La Laguna, 38205, Tenerife, Spain*
[c]*Department of Earth and Planetary Sciences, University of Tennessee, Knoxville, TN 37996, USA*
[d]*Laboratoire Lagrange, Observatoire de la Côte d'Azur, Nice, France*
[e]*of Central Florida, Physics Department, PO Box 162385, Orlando, FL 32816.2385, USA*
[f]*GTC Project, 38205 La Laguna, Tenerife, Spain*
[g]*INAF, Osservatorio Astrofisico di Torino, Pino Torinese, Italy*
[h]*Fundacin Galileo Galilei - INAF, La Palma, Spain*
[i]*Southwest Research Institute, Boulder, CO, USA*
[j]*MIT, Cambridge, MA, USA*

Abstract

Insert abstract text here

Keywords:

Asteroids, composition, Spectroscopy, Asteroids, dynamics

1. Introduction

The main asteroid belt, located between the orbits of Mars and Jupiter, is considered the principal source of near-Earth asteroids (Bottke et al., 2002). In particular the region bounded by two major resonances, the ν_6 secular resonance near 2.15 AU that marks the inner border of the main belt, and the 3:1 mean motion resonance with Jupiter at 2.5 AU. In this region, which we will call the inner belt, we can find several collisional families, with their members sharing dynamical properties, and a background of asteroids. In determining the origin of near-Earth asteroids (NEAs), collisional families are favored against isolated asteroids. NEAs have smaller diameters on average than asteroids from the main belt and

Email address: jmlc@iac.es (J. de León)

small asteroids are unlikely to be primordial objects but fragments of larger objects. In asteroid families numerous small fragments are produced during the family-forming event. Then those fragments spread over time primarily in semi-major axis due to the thermal forces of the Yarkovsky effect (which is more effective for small diameters) and some of them can drift into resonances and have their orbital parameters changed enough to reach the near-Earth space.

In the last years, the inner belt gained particular relevance since the two current targets of sample-return missions are believed to originate in that region. These are primitive NEAs (101955) Bennu, target of the NASA's OSIRIS-REx mission and (162173) 1999 JU_3, target of the Japanese Space Agency's Hayabusa-2 mission. Their most likely origin is in the primitive[1] collisional families of the inner belt, or even in the background, low-albedo population (Campins et al., 2010, 2013; Bottke et al., 2015). By 2012, there were four primitive families identified in the inner belt: Polana, Erigone, Sulamitis, and Clarissa (Nesvorný, 2012). In this work we focus in the Polana family.

The definition of collisional families evolves as new dynamical methods of classification appear and as more physical data on their members is known. The Polana family was initially defined as the low-albedo component of the Nysa-Polana complex (Cellino et al., 2001). In 2013 the Eulalia family was added by Walsh et al. (2013) and the Polana family changed to new Polana family. More recently, Milani et al. (2014) and Dykhuis & Greenberg (2015) describe a more complex picture, using the newly available color information from the Sloan Digital Sky Survey (Ivezić et al., 2002) and albedo information from the Wide-field Infrared Survey Explorer WISE/NEOWISE (Mainzer et al., 2011). While the former describe the Hertha-Polana-Burdett complex, and use WISE albedo information to identify the "dark" and "brigth" components of this complex as the Polana and Burdett families, the latter identifies a low-albedo family associated to Polana (similar to the one identified by Walsh et al. (2013)), and two other low-albedo families associated with (495) Eulalia. For the sake of

[1]Primitive families are those with asteroids having low albedos ($p_V \leq 0.1$) or primitive spectral types: B, C, and P taxonomical classes according to Tholen (1984) and Bus & Binzel (2002).

consistency, we will refer to the Polana-Eulalia complex or families following the most recent definition by Nesvorný et al. (2015).

We initiated a spectroscopic survey at the end of 2010 to study the primitive families located in the inner belt, starting with the Polana family. The final aim of this study was to characterize the primitive asteroid population in this region of the belt, and to better constrain the origin of asteroids (101955) Bennu and 1999 JU_3. Meanwhile, Walsh et al. (2013) identified two families of primitive asteroids in the region previously associated to the Polana family: the Eulalia family, with asteroid (495) Eulalia as the parent body, and the so-called new Polana family, with asteroid (142) Polana as the parent body. One of the conclusions of their work based on the spectroscopic information available by that time, was that near-infrared spectroscopy could help distinguishing both families. Asteroids from the new Polana family would have a red, positive spectral slope while asteroids from the Eulalia family would present a blue, negative spectral slope. Motivated by these new and very interesting dynamical findings, our group performed different observational campaigns to obatin both visible and near-infrared spectra of the asteroids in this region. Visible data was collected during two separate but coordinated observational campaigns, using the 10.4m Gran Telescopio Canarias (GTC) and the 3.6m Telescopio Nazionale Galileo (TNG), both located at the El Roque de los Muchachos Observatory (ORM), in the island of La Palma, and the 3.6m New Technology Telescope (NTT), located at La Silla Observatory, in Chile. In a companion paper we present the results obtained from the near-infrared spectra taken with the NASA's 3.0m Infrared Telescope Facility (IRTF) and the TNG (Pinilla-Alonso et al., Submitted). In this paper we present the results obtained from the visible spectra. In the following section we describe in detail the criteria used for the selection of the targets as well as the physical characteristics of the asteroids observed, including information like visible albedo and diameters. The observational procedures and the data reduction processes for the two campaigns are described in Section 3. We analyze the final reflectance spectra of the whole sample in Section 4 and we discuss the results in Section 5.

2. Selection criteria and sample description

As mentioned above, the data presented in this paper is a compilation of the visible spectra obtained during two separate but coordinated observational campaigns. The two datasets targeted the low-albedo ($p_V \leq 8\%$) and low-inclination ($i < 12^\circ$) asteroids of the so-called Polana-Eulalia family complex, and also included asteroids from the low-albedo and low-inclination background population. All these objects are primitive asteroids located in the inner belt, in the region between the ν_6 secular resonance (2.15 AU) and the 3:1 mean motion resonance (2.5 AU).

The list of objects observed with the 10.4 m Gran Telescopio Canarias (GTC) was prepared using the following procedure. We started with the members of the Nysa-Polana complex according to Nesvorný (2010). Then, using albedo values from WISE, we separated the members of the Polana family by selecting those with geometric albedo $p_V \leq$0.8. Polana members were also identified by their primitive SDSS colours or spectra. From the obtained list of objects, we selected those that had absolute magnitude $H > 15$ in order to focus on the smaller members of the family and to better exploit the capabilities of a 10.4m telescope like the GTC. A total of 30 asteroids were observed during this campaign.

The targets observed with the 3.6m Telescopio Nazionale Galileo (TNG) and New Techonology Telescope (NTT) were selected primarily to be located within the Yarkovsky boundaries of the Polana-Eulalia family complex. As defined by Walsh et al. (2013), objects from these families have a visible albedo $p_V \leq 0.1$. A total of 35 asteroids were observed during this campaign, with one of object observed twice (asteroid 6698).

The complete database analyzed in this paper contains 64 asteroids. For the purpose of our analysis, we separate the objects in members of the Polana and the Eulalia families, and objects from the low-albedo background. Membership criterium is based on values of the proper semi-major axis (a), proper eccentricity (e) and proper inclination (i) of the objects, as well as the location of the objects in the (a, H) space. Fig. 1 shows the proper orbital elements (a, e, and sine i) of the two families, Polana (light grey) and Eulalia (dark grey), together with the proper orbital elements of the asteroids observed in this work. Red, blue,

and green circles correspond to asteroids that are members of the Polana and the Eulalia families, and of the background population, respectively. The same color code applies for the objects in Fig. 2. In this (a, H) space, each family is bounded by its Yarkovsky lines or curves. This lines mark the location of a size-dependent envelope around the center of the family and represent the dispersion, due to the Yarkovsky effect of the fragments created after the collisional event that generated the family. Table[2] 1 shows, for each asteroid, its proper orbital elements taken from Asteroids Dynamic Site, its absolute magnitude H obtained from the Minor Planet Center, its visible albedo p_V and diameter D from WISE. For those objects that do not have a computed value of visible albedo we use the mean value for the corresponding taxonomic class from Mainzer et al. (2011), and the diameter is then computed using the formula $D = 1329\ p_V^{-1/2} 10^{-0.2H}$.

3. Observations and Data Reduction

Observational details for both campaigns are listed in Table 2. Information includes asteroid number, date of observation, starting UT and exposure time, telescope, airmass, and solar analog stars observed.

3.1. 10.4 m Gran Telescopio Canarias (GTC)

We obtained low- to intermediate-resolution spectroscopy for the presented sample using the Optical System for Imaging and Low Resolution Integrated Spectroscopy (OSIRIS) camera spectrograph (Cepa et al., 2000; Cepa, 2010) at the 10.4m Gran Telescopio Canarias (GTC), located at the "El Roque de los Muchachos" Observatory (ORM) in La Palma, Canary Islands, Spain. The OSIRIS instrument consists of a mosaic of two Marconi CCD detectors, each with 2048 x 4096 pixels and a total unvignetted field of view of 7.8 x 7.8 arcmin, giving a plate scale of 0.127 arcsec/pix. However, to increase the signal to noise for our observations we selected the 2 x 2 binning mode with a readout speed of 100 kHz (that has a

[2]Orbital and physical data of the asteroids have been obtained using the Minor Planet Physical Properties Catalogue (MP^{3}C) webpage, maintained by the Observatoire de la Cote d'Azur, http://mp3c.oca.eu/MP3C/

gain of 1.15 e-/ADU and a readout noise of 3.5 e-), as corresponds with the standard operation mode of the instrument. All the spectra were obtained using the OSIRIS R300R grism that produces a dispersion of 7.74 Å/pix, covering the 4800-10000 Å spectral range. A wide 5.0" slit width was used to account to possible variable seeing conditions and oriented at the parallactic angle to minimize slit losses due to atmospheric dispersion. For all the targets a series of three spectra were taken, with exposure times ranging from 200-300 s depending on the target brightness. Consecutive spectra were shifted in the slit direction by 10 arcsecs, in order to improve the sky subtraction and the fringing correction. Observations were done in service mode (within GTC program GTC44-12B) on different nights along September 2012-February 2013. Night conditions were rather variable, covering a wide range of different weather conditions. This was due to the fact that the program was classified as a "filler" (C-band) program within the GTC nightly operation schedule. The aim of this program was to obtain high signal-to-noise spectra for targets that are relatively bright for a 10m-class telescope (magnitudes up to 19) in non-optimal weather conditions, which include a high seeing value (larger than 1.5 arcsec), bright moon, or dense cirrus coverage. This results in spectra quality that can be very different from one night to another without direct relation to the target brightness, as the weather conditions (i.e. clouds, sky brightness, etc.) are the main constraint throughout the observations. Spectroscopic reduction has been done using the standard IRAF tasks. Images were initially bias and flat-field corrected, using lamp flats from the GTC Instrument Calibration Module. The two-dimensional spectra were then wavelength calibrated using Xe+Ne+HgAr lamps. After the wavelength calibration, sky background was subtracted and a one dimensional spectrum was extracted, using an extraction aperture that varied depending on the seeing of the corresponding night. To correct for telluric absorption and to obtain the relative reflectance, each observing night at least one solar analogue star from the Landolt list (Landolt, 1992) was observed using the same spectral configuration at an airmass similar to that of the object. When possible, more than one solar analogue star was observed in order to improve the final spectra quality. Each individual spectrum of the object was then divided by the corresponding spectrum of the

solar analogue, and then normalized to unity at 0.55 μm. The three individual spectra were averaged, obtaining the final reflectance spectra shown in Fig.A.10

3.2. 3.6 m Telescopio Nazionale Galileo (TNG) and New Technology Telescope (NTT)

Visible spectra at the TNG, also located at the ORM in La Palma, were obtained with the DOLORES spectrograph (Device Optimized for the LOw RESolution). The instrument is equipped with a 2048 x 2048 detector with a 0.25 "/pix plate scale, which yields a 8.6 x 8.6 arcmin field of view. The low resolution LR-B (blue) and LR-R (red) grisms were used, covering the 3000-8430 Å and the 4470-10073 Å spectral ranges, and with dispersions of 2.52 and 2.61 Å/pixel, respectively. A 1.5" slit was used oriented at the parallactic angle. For each grism only one spectrum of the object was obtained, starting always with the LR-B grism and then changing to LR-R grism. Table 2 shows the exposure time for each of the grisms (LR-B / LR-R). When only one value appears it means that the same exposure time was used for both grisms.

The NTT observations (La Silla Observatory, Chile) were performed using the EFOSC2 instrument (ESO Faint Object Spectrograph and Camera), equipped with a 2048 x 2028 CCD with a 0.12"/pixel plate scale, providing a 4.1 x 4.1 arcmin field of view. The disperser element was the Grism#1, which gives a dispersion of 6.6 Å/pixel and covers the 318510940 Å spectral range. We used a 2" slit, oriented along the parallactic angle for all objects. Observational details for both telescopes are listed in Table 2. Data reduction was done using IRAF. Images were corrected from bias and flat-field and then wavelength calibrated using HeAr calibration lamp for the NTT data and Ar+NeHg+Kr calibration lamps for both LR-B and LR-R grisms at the TNG. After the wavelength calibration, sky background was subtracted and a one dimensional spectrum was extracted. In order to remove the solar contribution, several solar analog stars around the time and airmass of the objects were observed each night. To obtain the final reflectance spectrum of each asteroid we divided their individual spectra by the corresponding spectra of the solar analog star, and the resulting spectra were then normalized to unity at 0.55 μm. The spectra are shown in Fig. A.10.

4. Results and Analysis

Our final sample contains visible spectra of a total of 64 asteroids, from which 36 (56%), 20 (31%), and 8 (13%) are members of the Eulalia and Polana families, and the background population, respectively. Based on the results obtained by Walsh et al. (2013), where they raise the possibility of using near-infrared spectroscopy to distinguish between Eulalia and Polana asteroids, we first compare the visible spectra of the asteroids in our sample to see if the same applies to visible wavelengths. Before doing this, we compare the visible spectra of the two parent bodies of the families, asteroids (142) Polana and (495) Eulalia.

4.1. Visible spectra of asteroids (142) Polana and (495) Eulalia

We found two visible spectra of asteroid (142) Polana published in the literature, one from Bus & Binzel (2002) in the frame of the SMASS-II survey, and the other from Vilas et al. (2006). A third spectrum was obtained using the NTT and is part of the sample studied this work. In the case of asteroid (495) Eulalia, there were also two previously published visible spectra, one from Xu et al. (1995), within the phase-I of the SMASS survey, and the other also from Vilas et al. (2006). A third spectrum of Eulalia was obtained by Vania Lorenzi using the TNG on the night of May 5, 2014 and is presented in this work. She used a similar configuration as that used for the asteroids observed with the TNG: DOLORES instrument and the two grisms, LR-B and LR-R, but with a 2" slit (see Section 3.2). For each of the grisms, three spectra of 600 seconds of exposure time each were obtained, moving the telescope 10" in the slit direction between individual exposures. Landolt star SA 102-1081 was used as solar analog. We followed the same procedure as that described in Section 3.2 to reduce the data. The visible spectra of (142) Polana and (495) Eulalia are shown in Fig. 3, normalized to unity at 0.55 μm and with a vertical offset for clarity. The mean visible spectra of the two asteroids is also shown in the figure. From a simple visual inspection, the three spectra of Polana look the same, all having blue, featureless negative spectral slopes. On the contrary, there are differences between the three spectra of Eulalia: both our spectrum and that of Vilas et al. (2006) have neutral to slightly red spectral slopes, while the one from Xu et al. (1995) is more similar to the spectra of Polana, having a blue spectral slope.

To perform a more quatitave comparison, we taxonomically classified all the spectra using the M4AST on-line tool (Popescu et al., 2012). The way this tool classifies an spectrum is quite simple: after uploading the data file to their web page[3] the tool fits a curve to the data and compares this curve with the taxons defined by DeMeo & Binzel (2009) at the corresponding wavelengths, using a χ^2 fitting procedure. The output consists of the best 5 results, in order of decreasing goodness of fit (increasing standard deviation). We show in Table 3 the first three results generated by the M4AST tool for all the individual spectra and for the mean spectrum of each of the asteroids. Additionally, we computed the spectral slope S' as defined by Luu & Jewitt (1990) in the 0.55-0.90 μm range, in units of %/1000Å. The resulting values and their associated errors are shown in the last two columns of Table 3. Asteroid (142) Polana is classified as a B-type and presents a negative spectral slope independently of the data source. In the case of Eulalia, there are more differences between the results obtained for the individual spectra, although in general one can say that this asteroid is a C-type. Nevertheless, caution must be taken when interpreting this results. As an example, take the values obtained for the visible spectrum of Eulalia from Vilas et al. (2006). The difference between the standard deviation from a C-type (4.1) and a B-type (4.8) is very small. This means that two spectra can be nearly identical, but due to the fact that formal classification uses a simple system of cutoffs to differentiate spectra, any minute variations in the two spectra can lead to different final taxonomies. We will keep this in mind when interpreting the results for the complete sample of asteroids presented in this work.

Comparing the spectral slopes of the two asteroids, both being negative, the value of (142) Polana is about six times larger than that of (495) Eulalia. However, the difference between the two spectral slopes (1.273 %/1000 Å) is just slightly larger than the value of 1 %/1000Å, which is the typical uncertainty in spectral slope introduced by the use of different solar analog stars (Lazzaro et al., 2004). Nevertheless, we conclude from this analysis that the final mean spectra of asteroids (142) Polana and (495) Eulalia are different and that

[3]http://cardamine.imcce.fr/m4ast/

Polana is a B-type and Eulalia is a C-type.

4.2. Spectral characteristics of the sample

The next step is to compare the visible spectra of the asteroids presented in this work to the visible spectra of (142) Polana and (495) Eulalia, and to confirm if they can be used to distinguish between members of the Polana and Eulalia families, or to the background population. To do this, we taxonomically classified each asteroid using the M4AST tool following the same procedure as that described in the previous section. In the same way, we computed the spectral slope S' in the 0.55-0.90 μm wavelength range for all the objects. The results of the classification procedure and the computed slopes are shown in Table 1.

As a first step, we plot the visible spectra of all the asteroids[4] in Fig. 4a (grey), together with the resulting mean spectrum of the sample and the lines corresponding to $\pm 1\sigma$ of the mean (black). We have also included for comparison the visible spectra of asteroids (142) Polana (blue) and (495) Eulalia (red). Fig. 4b is the same as Fig. 4a but after the application of a smoothing factor of 50 to the spectra, for a better visualization. From a visual inspection, the mean spectrum of the sample is similar to the spectrum of Eulalia, although the spectrum of Polana is marginally in the limits imposed by the $\pm 1\sigma$ of the mean. As describied in Section 2, we separated our objects in three groups, attending to their membership to the Polana and Eulalia families, or to the background population, and computed the mean spectrum of each of the groups. Fig. 4c shows the resulting mean spectrum of the Polanas (blue), Eulalias (red), and background objects (green), together with the mean spectrum of the whole sample (black). Again, Fig. 4d is the same as Fig. 4c but with a smoothing factor of 50. In this case, the three mean spectra and the mean spectrum of the sample are identical within the uncertainties, sugessting that it is not possible to distinguish between a member of the Polana or Eulalia families using visible spectra.

Fig. 5 shows the distribution of the spectral slopes of the three groups, Polanas (blue), Eulalias (red) and background population (green). The mean spectral slope of the sample

[4]The visible spectrum of each of the asteroid studied in this work can be seen in Fig. A.10.

is S' = -0.411 ± 0.331 %/1000Å, ranging[5] from quite blue (-2.939 %/1000Å) to moderately red (2.717 %/1000Å). This spectral slope variation is real, as it is significantly larger than the observed dispersion in the slope of the solar analogs used to reduce the data (always smaller than 1%/1000Å). The slope distributions of the three groups are very similar, having mean values of $S'_{Pol} = -0.707 \pm 0.211$ %/1000Å, $S'_{Eul} = -0.472 \pm 0.138$ %/1000Å, and $S'_{Back} = -0.053 \pm 0.163$ %/1000Å. The dashed lines in Fig. 5 correspond to the spectral slope of asteroids Polana and Eulalia, shown in Table 3. As it can be seen, the three groups present spectral slopes which are very similar to each other, confirming the result presented above that it is not possible to distinguish if an asteroid belongs to one group or another based only on its visible spectrum.

Interestingly, the three groups present spectral slopes which are very similar to that of (495) Eulalia, while the spectrum of asteroid (142) Polana is bluer than the mean spectrum of the sample, and presents a more negative spectral slope, even when compared to the asteroids of the Polana family. This difference in slope still lies within the range of slope variation observed for the whole sample, but might be indicating that asteroid (142) is not the parent body of the Polana family. Instead, all the asteroids in the region of the Polana-Eulalia complex, including the background population, have similar visible spectra, and they are all similar to the visible spectrum of (495) Eulalia, suggesting that this asteroid could be the parent body of the two families.

Differences between the visible spectrum of the parent body of a family and the members of the family have been observed for other families, as is the case of the Pallas family (de León et al., 2010). In this particular case, those differences were explained by the difference in size between Pallas, with a diameter of $\sim$ 550 km, and its family members, with diameters ranging from 5 to 26 kms. Several studies on carbonaceous chondrites (Johnson & Fanale, 1973; Shepard et al., 2008) show that their visible spectra get bluer and darker with coarser

[5]Here we have excluded the value -4.783 %/1000Åwhich corresponds to asteroid 6815 (background population), as its spectrum shows a drop-off beyond 0.7 μm which we believe is due to some artifact in the observation.

grain size. Therefore it is possible that large objects are covered by dusy, fine regoligh, while smaller objects could have lost their regolith during the collisional event that created them, preserving preferentially larger grains, and showing bluer spectra. This effect could explain why the visible spectrum of asteroid (142) Polana is bluer than the spectra of the member of the family. Fig. 6 shows the distribution of the sizes of the members of the Polana and Eulalia families, and of the background population. The members of the Polana family studied here have diameters which range from 5 to 30 km, having a mean diameter of 10 km, which is of the order of the size of Polana ($D \sim 56$ km). Therefore, differences in size can not be used to explain the difference in the spectra between Polana and its family members.

4.3. Taxonomical analysis

Fig. 7 shows the distribution of taxonomic classes among the three groups, Polanas, Eulalias and background objects. There are no significant differentes between the two families, both having almost equal numbers of C- and B-types. Only one asteroid has been classified as an S-type, clearly an interloper. Considering the sample as a whole, the two primitive classes are even more equally distributed, with 51% of C-types and 42% of B-types. Although one might be tempted to say that we have two distinct taxonomical groups in the region, it is important to note here that, for example, a small difference in spectral slope is enough to change the classification from one type to the other. This is well illustrated in Table 1, where the majority of the asteroids classified as B-types, have C-type as the second best fit. Therefore, we can conclude that we do not see any significant difference in terms of taxonomical classes between the Polanas, Eulalias or the background population, in agreement with the results obtained from the analysis of their visible spectra.

4.4. Comparison with targets of space missions: (101955) Bennu and 1999 JU_3

While the work presented here focuses on the Polana-Eulalia complex, it is part of a more general study, a coordinated effort to characterize the surface composition of primitive asteroids in the inner belt. The final aim of this study was to characterize the primitive asteroid population in this region of the belt, and to better constrain the origin of asteroids

(101955) Bennu and 1999 JU_3. These are near-Earth asteroids considered as primary targets of the NASA's OSIRIS-REx (Lauretta et al., 2010) and JAXA's Hayabusa 2 (Tsuda et al., 2013) sample return missions, respectively.

- (101955) Bennu. This near-Earth asteroid has been extensively studied. Its visible and near-infrared spectrum indicates it has a primitive composition, resembling spectra of carbonaceous chondrites. Campins et al. (2010) place the origin of Bennu in the inner asteroid belt, in particular in the Polana family, while a more recent work by Bottke et al. (2015) considers the background primitive population of the inner belt as the most likely origin of this asteroid. In Fig. 8 we compare the visible spectrum of Bennu from Clark et al. (2010) and its visible colors from Hergenrother et al. (2013) with the spectra of asteroids (142) Polana and (495) Eulalia (left panel), and with the mean spectra of the Polanas, the Eulalias, and the background population, as described in Section 4.2 (right panel). Visible spectrum of Bennu ($S' = -1.280 \pm 0.033$ %/1000Å) is almost identical to the visible spectrum of asteroid (142) Polana ($S' = -1.526 \pm 0.028$ %/1000Å), something that was already noticed by Campins et al. (2010) and that supported their conclusion of the Polana family as the most likely source region of Bennu. As in the case of the spectrum of Polana, the spectrum of Bennu is different from the mean spectra of any of the three groups studied in this work, although it lies in the boundaries defined by the $\pm 1\sigma$ of the mean spectrum of the whole sample. Visible colors ($S' = -0.766 \pm 0.030$ %/1000Å) from Hergenrother et al. (2013) are more or less in between the spectra of Polana ($S' = -1.526 \pm 0.028$ %/1000Å) and Eulalia ($S' = -0.253 \pm 0.057$ %/1000Å), and in this sense are more compatible with the spectra of the asteroids of the Polana-Eulalia complex ($S'_{Pol} = -0.707 \pm 0.211$ %/1000Å, $S'_{Eul} = -0.472 \pm 0.138$ %/1000Å).

- (162173) 1999 JU_3. There are multiple references in the literature to visible spectra of this near-Earth asteroid. The first spectrum was published by Binzel et al. (2001), showing an ultraviolet drop-off in reflectance short-wards 0.65 μm and giving a classification as a Cg-type. Two other visible spectra were published by Vilas (2008), and

were obtained on July and September 2007. The two spectra were different from each other, and also different from the one by Binzel et al. (2001), showing no ultraviolet drop-off. The spectrum obtained in July showed an absorption band at 0.7 μm and a red spectral slope, while the one obtained in September, with a much higher signal-to-noise, presented a neutral slope and showed no absorption bands. A comparison between these three spectra can be seen in Fig. 3 from Campins et al. (2013). Additional rotationally resolved visible spectra of 1999 JU_3 were presented by Lazzaro et al. (2013), Moskovitz et al. (2013), and Sugita et al. (2013), all of them compatible with a C-type classification and showing no absorption feature at 0.7μm and a spectral slope similar to the September spectrum from Vilas (2008). This visible spectrum is also compatible with the available near-infrared spectra of this asteroid. Being the one with the highest signal-to-noise, we have selected it to perform our spectral analysis.

Therefore we compare in Fig. 9 the selected visible spectrum of 1999 JU_3 with the visible spectra of asteroids Polana and Eulalia, and with the mean spectra of the Polanas, Eulalias, and background population, as we did for asteroid Bennu. The spectrum of 1999 JU_3 is in good agreement ($S' = 0.958 \pm 0.198$ %/1000Å) with any of the three populations, being more similar to the mean spectra of the Background population ($S'_{Back} = -0.053 \pm 0.163$ %/1000Å), and showing a considerable difference from the spectrum of asteroid (142) Polana. This result is in good agreement with the findings by Campins et al. (2013), which place the most likely origin of asteroid 1999 JU_3 in the low-albedo and low-inclination region of the inner belt.

5. Conclusions

From the results obtained in the previous section, we can say here that the dynamical complexity observed in the region of the Polana-Eulalia complex does not translate into spectral complexity. We have analyzed the visible spectra of a total of 64 low-albedo asteroids, members of the Polana and Eulalia families, and from the background population. Their visible spectra show a continuum from blue to moderately red typical of primitive asteroids

classified as B- and C-types. Visible spectra of the asteroids studied here can not be used to distinguish between members of any of the three groups, having all similar spectra. This spectral homogeneity suggests compositional homogeneity in the low-albedo population of this region of the inner belt, and it is compatible with our results based on near-infrared spectra (Pinilla-Alonso et al., 2015). The Pinilla-Alonso et al. (2015) near-infrared spectroscopic survey samples the same region of low albedo asteroids, and also finds spectral homogeneity within the dispersion of the slopes within the C- or B- taxonomical classes, typically associated to primitive surfaces. Then, is it possible to have two dynamical families, located so close and with the same composition? One hypothesis to explain this compositional homogeneity observed both in the visible and the near-infrared is that only one asteroid is responsible for the generation of the objects in this region: one original primitive parent body that disintegrated after a catastrophic collision into several large fragments and then some smaller pieces that comprise the different families identified so far. Interestingly, the behaviour of the visible spectrum of asteroid (142) Polana (bluer than the mean spectrum of the sample and the spectrum of Eulalia), is repeated in the near-infrared: in that wavelength region, the spectrum of (142) Polana lies in the boundaries defined by the $\pm 1\sigma$ of the mean spectrum of the sample, but still is redder than the mean and also redder than Eulalia. This result might support our interpretation that asteroid (495) Eulalia could be the parent body of the asteroids of the two families.

More dynamical studies are needed to confirm this hypothesis but what is clear at this moment is there is a large component of low albedo asteroids in the inner belt, that is strongly perturbed by the ν_6 and 3:1 resonances and that is formed by asteroids classified as B or C-type (from visible observations) with a neutral to moderately red concave-up spectra in the near-infrared. Our results also support that the two near-Earth asteroids which are visited by space missions in the next decade most likely originate in this region of the inner belt.

Acknowledgments

PLEASE CHECK YOUR ACKNOWLEDGEMENTS!!! *JdL* acknowledges sup-

port from the Insituto de Astrofísica de Canarias. *NPA* work was partial funded by the 'Gaia Research for European Astronomy Training' (GREAT) of the ESF Research Networking Programmes, under a short-visit grant. *HC* acknowledges support from NASA's Near-Earth Object Observations program and from the Center for Lunar and Asteroid Surface Science funded by NASA's SSERVI program at the University of Central Florida. *HC* was a visiting astronomer at the Observatoire de Paris and at the Observatoire de la Côte d'Azur, in France, funded by a grant from the European Science Foundation's Gaia Research for European Astronomy Training.*FED* acknowledges support through NASA Grant No. NNX12AL26G issued through the Planetary Astronomy Program.

Table 1: Physical and dynamical properties of the asteroids studied in this paper. The information includes proper semi-major axis, eccentricity, and sine of the inclination, absolute magnitude, WISE visible albedo, diameter, spectral slope, and taxonomical classification

Asteroid	a (AU)	e	sine i	H	p_V	err p_V	D (km)	err D	S' (%/1000 Å)	err S'	Taxonomy M4AST		
142	2.418	0.158	0.056	10.27	0.0447	0.0059	56.56	1.40	-1.166	0.059	B	Ch	C
1183	2.384	0.157	0.047	12.30	0.0337	0.0009	25.16	0.07	-1.331	0.128	B	Ch	C
1768	2.450	0.155	0.055	12.70	0.0316	0.0067	20.22	0.13	-1.230	0.076	B	Ch	C
2081	2.450	0.152	0.054	12.14	0.0678	0.0083	16.67	0.10	-0.359	0.138	Ch	C	B
2279	2.460	0.187	0.042	12.97	0.0438	0.0017	14.84	0.05	-1.418	0.043	B	Ch	C
3130	2.466	0.160	0.057	13.00	0.0554	0.0053	13.11	0.10	-0.941	0.182	B	Ch	C
3185	2.366	0.153	0.054	13.60	0.0500	0.0075	9.42	0.23	-0.531	0.253	C	Ch	Cb
					0.038	0.0037	10.29	0.16					
3298	2.354	0.152	0.061	13.60	0.0632	0.0093	10.54	0.12	-1.420	0.143	B	Ch	C
3485	2.440	0.149	0.044	12.80	0.0481	0.0028	15.24	0.08	-0.753	0.100	B	Ch	C
4173	2.359	0.154	0.059	13.50	0.0594	0.0015	11.75	0.05	-2.738	0.310	B	Ch	C
5158	2.424	0.145	0.046	14.20	0.0750*	0.0100*	7.01	0.62	-1.733	0.317	B	Ch	C
6578	2.422	0.157	0.054	14.30	0.0614	0.0050	7.87	0.03	2.717	0.247	Xc	X	Xk
6142	2.460	0.158	0.054	13.40	0.0750*	0.0100*	10.14	0.90	-1.373	0.262	B	Ch	C

Table 1: continued.

Asteroid	a (AU)	e	sine i	H	p_V	err p_V	D (km)	err D	S' (%/1000 Å)	err S'	Taxonomy M4AST		
6661	2.376	0.148	0.053	13.50	0.0750*	0.0100*	9.68	0.86	-0.916	0.333	B	Ch	C
6698 (1)	2.441	0.152	0.047	14.20	0.0478	0.0046	8.52	0.07	-0.239	0.261	C	Ch	B
6698 (2)	2.441	0.152	0.047	14.20	0.0478	0.0046	8.52	0.07	-0.427	0.451	C	Ch	B
6769	2.416	0.148	0.055	13.60	0.0580*	0.0100*	10.52	1.10	1.405	0.629	Cb	C	Cgh
6815	2.432	0.159	0.045	14.50	0.0750*	0.0100*	6.11	0.54	-4.783	0.324	B	O	Ch
6840	2.429	0.145	0.048	14.30	0.0428	0.0077	8.56	0.03	-0.185	0.192	Ch	Cb	C
7078	2.435	0.187	0.044	13.90	0.0954	0.0195	8.99	0.15	-0.212	0.107	Ch	C	Cb
9052	2.464	0.152	0.051	14.00	0.0676	0.0020	8.09	0.03	0.643	0.175	Cb	C	Ch
10866	2.431	0.158	0.057	14.60	0.0529	0.0069	6.41	0.06	-1.468	0.239	B	Ch	C
14849	2.371	0.158	0.053	14.80	0.0444	0.0299	7.21	2.20	-1.913	0.729	B	Ch	C
15794	2.432	0.159	0.050	14.40	0.0707	0.0177	6.90	0.16	-1.144	0.337	B	Ch	C
20843	2.395	0.148	0.047	14.80	0.0392	0.0062	6.54	0.12	0.261	0.090	Cb	C	Ch
21176	2.454	0.154	0.050	14.40	0.0500	0.0033	7.65	0.06	-1.210	0.095	B	Ch	C
23270	2.459	0.161	0.051	15.00	0.0367	0.0038	5.51	0.31	-0.523	0.137	Cb	B	Ch
24650	2.394	0.145	0.048	15.00	0.0267	0.0042	6.16	0.14	-0.316	0.051	C	Ch	Cgh
25490	2.427	0.150	0.049	14.70	0.0610	0.0095	6.59	0.12	1.653	0.571	Cb	C	Xk
27354	2.418	0.148	0.043	14.50	0.0360	0.0073	7.33	0.21	0.169	0.080	C	Cb	Cg
29626	2.412	0.149	0.047	15.40	0.0740*	0.0100*	4.06	0.33	2.010	0.0049	Xc	Xk	Cb

Table 1: continued.

Asteroid	a (AU)	e	sine i	H	p_V	err p_V	D (km)	err D	S' (%/1000 Å)	err S'	Taxonomy M4AST		
30043	2.402	0.186	0.048	15.80	0.0780	0.0365	3.45	1.36	-1.226	0.141	Cg	Cgh	Ch
32847	2.400	0.141	0.049	14.50	0.0578	0.0035	7.74	0.11	0.807	0.308	C	Cb	Cg
33804	2.398	0.145	0.048	14.80	0.0750*	0.0100*	5.32	0.47	-0.936	0.327	B	Ch	C
34326	2.413	0.144	0.045	14.60	0.0439	0.0065	6.64	0.10	-0.317	0.220	B	Ch	C
36465	2.395	0.153	0.054	15.50	0.0516	0.0054	3.73	0.53	0.374	0.204	Ch	Cgh	C
					0.0876	0.0143	4.87	0.36					
36469	2.389	0.155	0.058	15.30	0.0464	0.0069	4.90	0.23	1.380	0.117	Cb	C	Ch
					0.0448	0.0047	4.99	0.10					
37354	2.411	0.145	0.055	14.40	0.0734	0.0093	6.47	0.22	-0.258	0.729	C	Ch	Cb
39888	2.420	0.145	0.045	15.30	0.0750*	0.0100*	4.23	0.34	-1.096	0.153	B	Ch	C
41525	2.392	0.163	0.041	15.90	0.0642	0.0155	3.80	0.22	-1.161	0.300	B	Ch	C
42006	2.467	0.146	0.042	15.30	0.0758	0.0300	4.45	0.15	0.223	0.345	C	Cgh	Ch
					0.1292	0.0156	5.81	0.15					
45846	2.415	0.149	0.049	15.20	0.0580*	0.0100*	5.03	0.53	-0.269	0.417	Ch	B	C
49833	2.418	0.156	0.056	15.50	0.0580*	0.0100*	4.38	0.46	0.075	0.211	Cb	C	Ch
53170	2.391	0.145	0.045	14.80	0.0495	0.0087	6.32	0.09	-0.936	0.120	Cgh	Cg	Ch
53918	2.375	0.149	0.048	15.60	0.0497	0.0042	4.52	0.14	-2.939	0.247	Cg	Q	Cgh
57068	2.362	0.155	0.047	16.40	0.0549	0.0140	2.98	0.10	-1.767	0.144	B	C	Cg

Table 1: continued.

Asteroid	a (AU)	e	sine i	H	p_V	err p_V	D (km)	err D	S' (%/1000 Å)	err S'	Taxonomy M4AST		
59317	2.396	0.157	0.057	15.90	0.0530	0.0119	4.00	0.08	-0.852	0.391	B	C	Cb
59322	2.440	0.171	0.044	15.60	0.0580	0.0100	4.19	0.41	0.771	0.237	Cg	Xk	C
59397	2.437	0.176	0.046	15.20	0.1976	0.0214	2.85	0.19	0.978	0.242	Cb	C	Xk
60571	2.392	0.148	0.046	15.60	0.0376	0.0083	4.97	0.21	-2.276	0.219	B	Ch	C
61500	2.403	0.146	0.047	15.70	0.0580*	0.0100*	4.00	0.42	0.753	0.718	Ch	C	Cb
61560	2.381	0.147	0.045	15.80	0.0580*	0.0100*	3.82	0.40	-0.069	0.276	Ch	C	Cgh
66333	2.373	0.139	0.046	15.50	0.0388	0.0051	4.67	0.11	-1.812	0.150	B	Ch	C
67352	2.361	0.156	0.043	16.00	0.0452	0.0053	3.44	0.08	-0.997	0.282	Q	Cg	C
80789	2.384	0.143	0.048	15.40	0.0459	0.0047	4.93	0.13	-0.702	0.178	Cg	Cgh	C
80993	2.369	0.142	0.042	16.00	0.0381	0.0038	4.50	0.19	-1.161	0.084	B	C	Ch
90975	2.352	0.141	0.049	16.30	0.0580 *	0.0100*	3.03	0.30	0.603	0.296	C	Cb	Cgh
93347	2.449	0.154	0.042	15.50	0.0696	0.0090	4.19	0.16	-1.381	0.164	B	Ch	C
109030	2.404	0.154	0.051	16.40	0.0447	0.0085	3.45	0.19	-0.642	0.218	Cg	Cgh	C
120190	2.369	0.157	0.047	16.10	0.0555	0.0187	3.56	0.34	2.671	0.214	X	Xc	Xk
120384	2.346	0.149	0.047	16.70	0.0500	0.0048	2.84	0.32	-0.938	0.221	C	B	Cg
126046	2.407	0.166	0.044	16.60	0.0580*	0.0100*	2.64	0.26	1.170	0.287	Cb	C	Ch
132091	2.347	0.149	0.048	16.10	0.0826	0.0188	2.92	0.62	-1.059	0.280	B	Ch	C
					0.0445	0.0120	3.98	0.47					

Table 1: continued.

Asteroid	a (AU)	e	sine i	H	p_V	err p_V	D (km)	err D	S' (%/1000 Å)	err S'	Taxonomy M4AST		
147535	2.358	0.150	0.048	15.80	0.0574	0.0057	3.84	0.17	0.518	0.072	C	Cg	Cgh
153694	2.298	0.129	0.049	16.90	0.0580*	0.0100*	2.30	0.24	-0.081	0.613	Ch	B	C

* Note: mean value of visible albedo for the corresponding taxonomic class, taken from Mainzer et al. (2011).

For these cases, asteroids diameters are computed using the expression indicated in Section 2.

Table 2: Summary of the observational circumstances of the asteroids presented in this paper.

Asteroid	Date	UT start	Exp. time (s)	Telescope	Airmass	Solar analog*
142	2011-07-20	23:51	2 x 240	NTT	1.06	5, 7, 8
1183	2011-07-21	00:01	2 x 600	NTT	1.27	5, 7, 8
1768	2011-07-22	09:46	2 x 900	NTT	1.16	5, 6, 7, 8
2081	2011-07-21	01:59	1 x 600	NTT	1.37	5, 7, 8
2279	2012-12-30	20:08	3 x 250	GTC	1.01	2
3130	2011-07-21	03:21	2 x 900	NTT	1.25	5, 7, 8
3185	2011-07-23	XXX	XXX	NTT		
3298	2011-07-21	23:34	4 x 900	NTT	1.08	5, 6, 7, 8
3485	2010-10-31	00:00	600	TNG	1.09	1, 2, 7
4173	2011-07-22	01:27	5 x 900	NTT	1.22	5, 6, 7, 8
5158	2010-11-13	04:46	1800	TNG	1.06	1, 2
6142	2010-11-11	01:18	1500	TNG	1.07	1, 2
6578	2010-11-10	22:49	1200	TNG	1.21	1, 2
6661	2010-10-31	05:24	600	TNG	1.10	1, 2, 7
6698	2010-10-31	01:14	600	TNG	1.11	1, 2, 7
	2010-11-11	23:23	1200	TNG	1.07	1, 2, 7
6769	2010-11-11	04:04	1150/1200	TNG	1.01	1, 2
6815	2010-11-12	03:06	1800	TNG	1.01	1, 2, 7
6840	2010-11-11	22:07	1600/1800	TNG	1.15	1, 2, 7
7078	2011-07-21	02:29	3 x 600	NTT	1.13	5, 7, 8
9052	2010-11-11	20:46	1800	TNG	1.13	1, 2, 7
10866	2011-07-22	04:43	4 x 900	NTT	1.02	5, 6, 7, 8
14849	2011-07-22	23:26	4 x 900	NTT	1.10	5, 6, 7, 8
15794	2011-07-23	02:45	3 x 900	NTT	1.15	5, 6, 7, 8
20843	2013-01-15	06:35	3 x 300	GTC	1.38	4

Table 2: continued.

Asteroid	Date	UT start	Exp. time (s)	Telescope	Airmass	Solar analog*
21176	2013-01-15	03:02	3 x 300	GTC	1.06	4
23270	2013-01-19	06:39	3 x 350	GTC	1.16	4
24650	2012-09-18	00:26	3 x 200	GTC	1.31	2, 7
25490	2010-11-10	23:58	1500	TNG	1.35	1, 2
27354	2012-09-13	23:05	3 x 200	GTC	1.57	7
29626	2012-09-13	22:02	3 x 250	GTC	1.50	7
30043	2012-09-18	21:45	3 x 250	GTC	1.43	2, 7
32847	2011-07-21	07:35	2 x 900	NTT	1.13	5, 7, 8
33804	2010-11-13	01:35	1800	TNG	1.04	1, 2
34326	2011-07-21	05:55	4 x 900	NTT	1.03	5, 7, 8
36465	2012-12-23	03:59	3 x 300	GTC	1.10	3
	2011-07-23	08:20	2 x 900	NTT	1.18	5, 6, 7, 8
36469	2013-01-15	02:23	3 x 300	GTC	1.14	4
37354	2011-07-23	01:03	4 x 900	NTT	1.05	5, 6, 7, 8
39888	2013-01-15	03:49	3 x 300	GTC	1.04	4
41525	2011-07-22	06:39	4 x 900	NTT	1.16	5, 6, 7, 8
42006	2011-07-23	09:08	4 x 900	NTT	1.23	5, 6, 7, 8
45846	2011-07-22	08:31	3 x 900	NTT	1.24	5, 6, 7, 8
49833	2010-11-12	00:45	1800	TNG	1.07	1, 2, 7
53170	2012-09-17	04:00	3 x 200	GTC	1.05	2, 7, 8
53918	2012-09-16	21:53	3 x 250	GTC	1.63	2, 7, 8
57068	2012-09-14	2356	3 x 250	GTC	1.42	7, 8
59317	2012-09-18	02:46	3 x 300	GTC	1.20	2, 7
59322	2012-09-17	00:39	3 x 250	GTC	1.30	2, 7, 8
59397	2012-09-17	03:22	3 x 300	GTC	1.09	2, 7, 8
60571	2012-10-09	00:34	3 x 250	GTC	1.32	8

Table 2: continued.

Asteroid	Date	UT start	Exp. time (s)	Telescope	Airmass	Solar analog*
61500	2011-07-23	05:09	4 x 900	NTT	1.16	5, 6, 7, 8
61560	2011-07-21	08:50	5 x 900	NTT	1.30	5, 7, 8
66333	3013-01-03	03:02	3 x 300	GTC	1.06	3
67352	2012-09-13	23:46	3 x 250	GTC	1.67	7
80789	2012-09-16	22:44	3 x 200	GTC	1.46	2, 7, 8
80993	2012-09-14	23:04	3 x 200	GTC	1.45	7, 8
90975	2013-01-09	01:52	3 x 300	GTC	1.18	2, 3
93347	2012-09-18	03:27	3 x 300	GTC	1.12	2, 7
109030	2012-09-15	21:05	3 x 300	GTC	1.59	7
120190	2012-09-17	23:41	3 x 300	GTC	2.08	2, 7
120384	2012-09-14	21:30	3 x 300	GTC	1.41	7, 8
126046	2012-10-19	02:41	3 x 250	GTC	1.09	8
132091	2013-01-09	06:05	3 x 400	GTC	1.08	2, 3
147535	2012-09-14	22:40	3 x 200	GTC	1.54	7, 8
153694	2011-07-23	04:06	5 x 900	NTT	1.09	5, 6, 7, 8

* (1) Hyades 64; (2) L93-101; (3) L98-978; (4) L102-1081; (5) L107-998; (6) L110-361; (7) L112-1333; (8) L115-271

Table 3: Taxonomical classification and spectral slopes of the visible spectra of asteroids (142) Polana and (495) Eulalia. The values in parentheses correspond to the standard deviation of the χ^2 fit for each taxonomic class

Data source	Taxonomy (χ^2x10^{-4})			S' (%/1000 Å)	err S'
Polana (SMASS-II)	B (46.9)	Ch (17.8)	C (29.3)	-2.218	0.055
Polana (Vilas)	B (4.2)	Ch (7.7)	C (20.4)	-1.233	0.042
Polana (this work)	B (2.9)	Ch (4.6)	C (7.3)	-1.166	0.059
Polana (mean)	**B** (1.9)	Ch (6.7)	C (17.0)	**-1.526**	**0.028**
Eulalia (SMASS-I)	B (2.7)	Ch (8.9)	C (17.3)	-0.708	0.049
Eulalia (Vilas)	Ch (3.0)	C (4.1)	B (4.8)	-0.428	0.139
Eulalia (this work)	C (0.7)	Cb (1.2)	Ch (6.9)	0.429	0.046
Eulalia (mean)	**Ch** (1.1)	Cb (3.2)	C (3.5)	**-0.253**	**0.057**

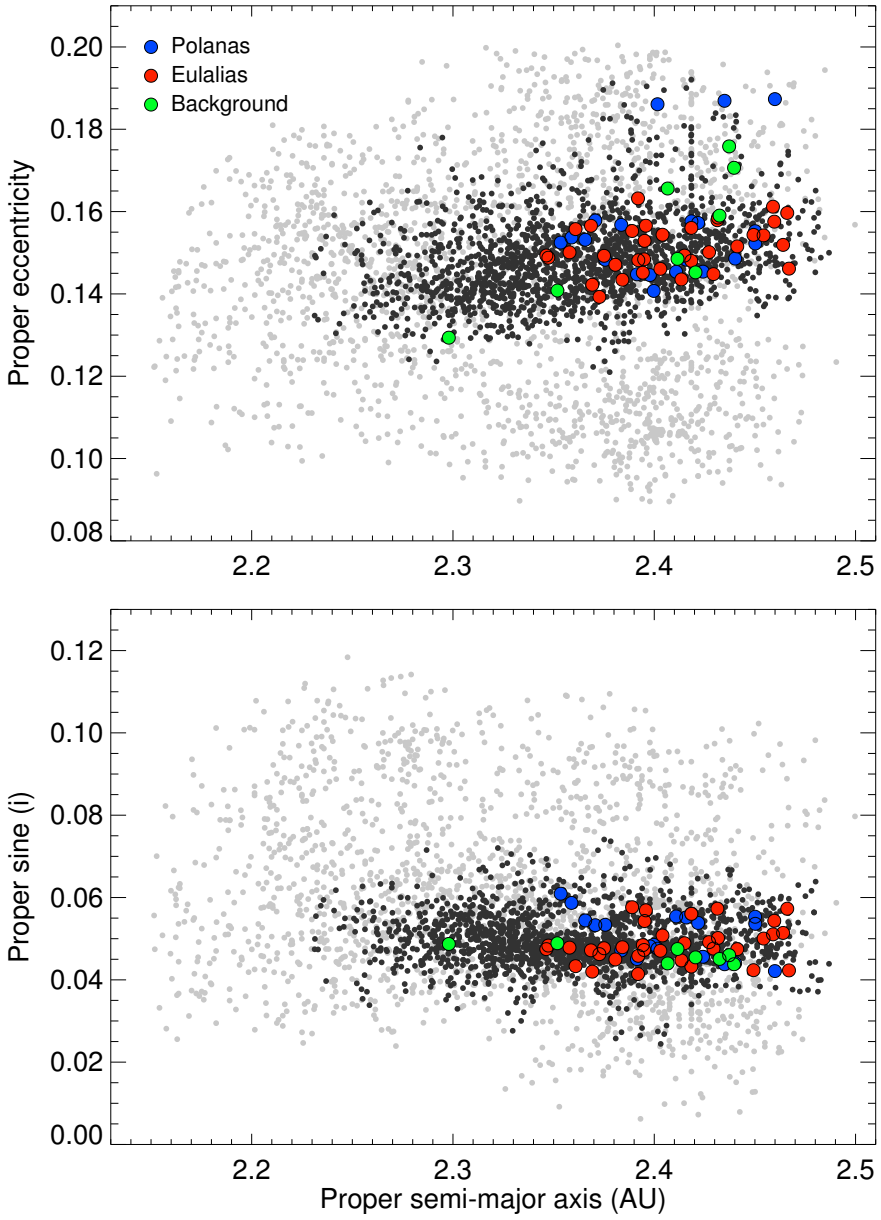

Figure 1: Proper orbital elements (semi-major axis, eccentricity, and sine of inclination) of the asteroids of the Polana (light grey) and Eulalia (dark grey) families, as defined by Walsh et al. Walsh et al. (2013). The color circles correspond to the asteroids observed in this work, according to their membership to the Polana (blue) and Eulalia (red) families, or to the background population (green).

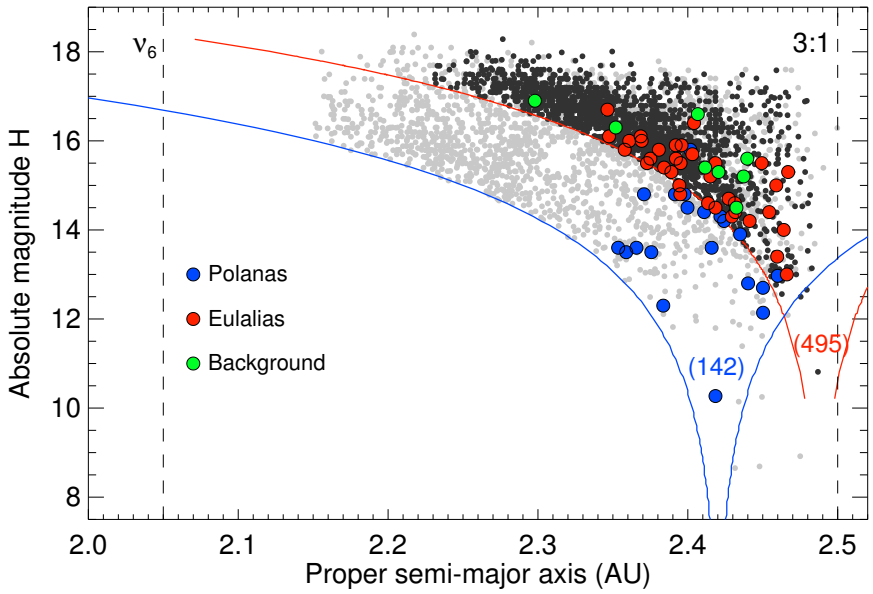

Figure 2: Semi-major axis (a) versus absolute magnitude (H) for all the asteroids presented in this paper. Objects from both Polana (light gray) and Eulalia (dark gray) families are included. Solid lines correspond to the boundaries of the Polana (blue) and Eulalia (red) families. The color circles correspond to the asteroids observed in this work, according to their membership to the Polana (blue) and Eulalia (red) families, or to the background population (green).

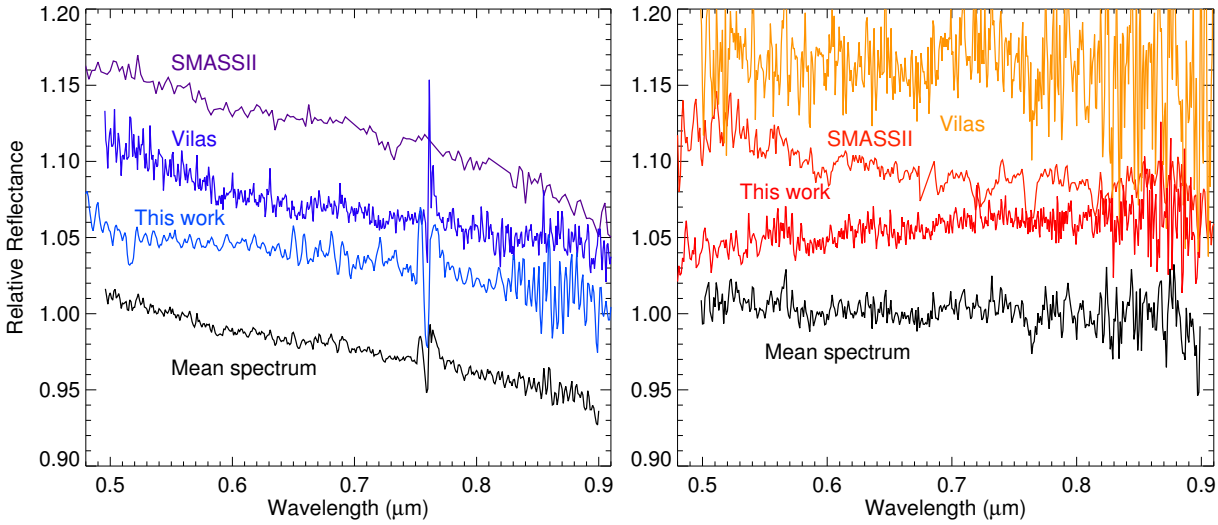

Figure 3: Visible spectra of asteroids (142) Polana and (495) Eulalia. We present the existent individual spectra, shifted vertically for clarity, together with the computed mean spectrum for each asteroid. All the visible spectra are normalized to unity at 0.55 μm.

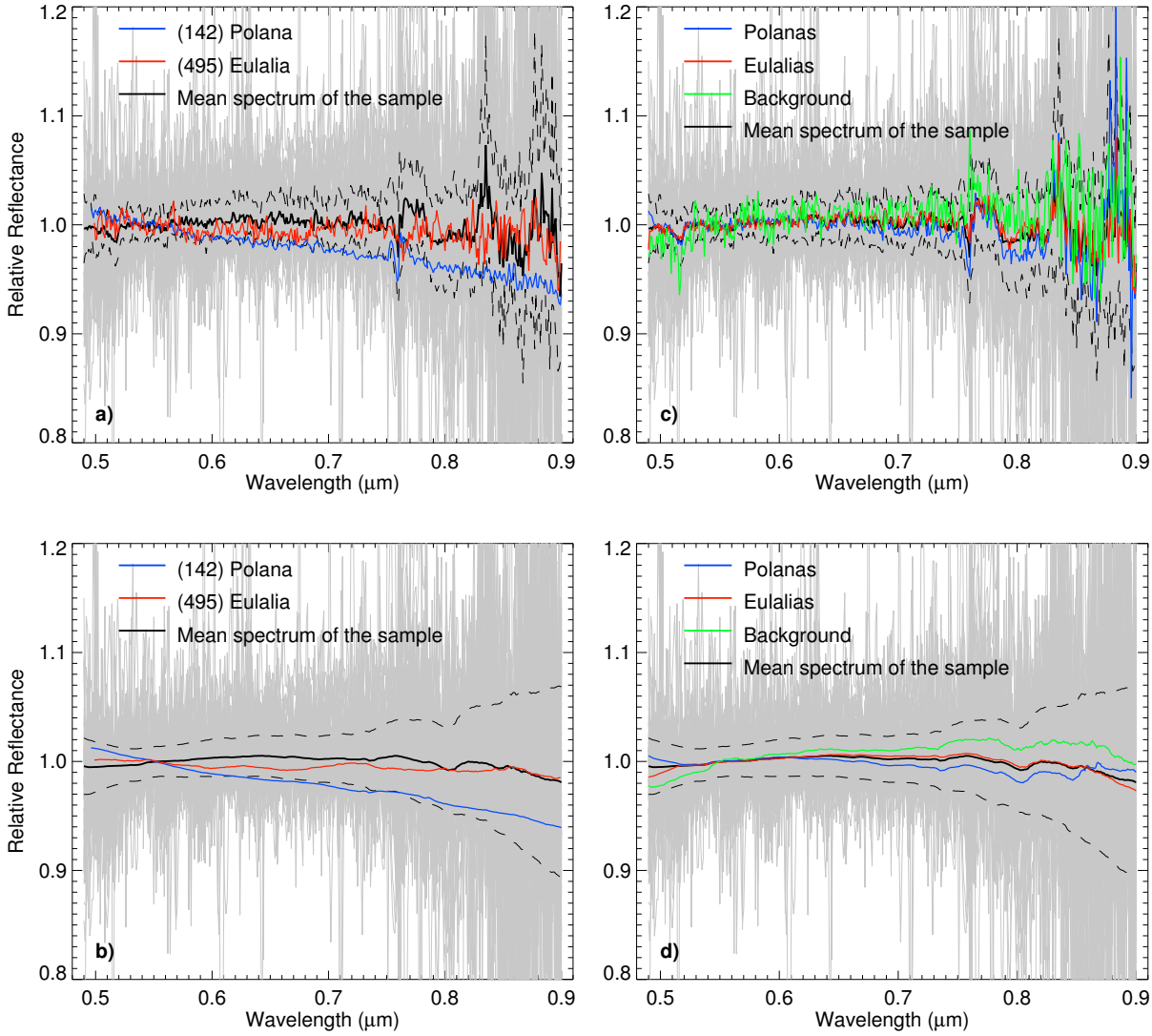

Figure 4: Visible spectra of the asteroids presented in this work. **a)**. Visible spectra of the whole sample (grey) and its mean spectrum (red), together with the $\pm$ 1σ of the mean (red dashed lines). We show the spectra of both asteroids, (142) Polana (blue) and (495 Eulalia (purple).**b)**. Same as a) but with a smoothing factor of 50 applied for better comparison. **c)**. Similar to a), but in this case we show the mean spectrum of the asteroids assigned to the Polana (blue) and Eulalia (purple) families, and to the background population (green). **d)**. Same as c) but witha a smoothing factor of 50 applied for better comparison.

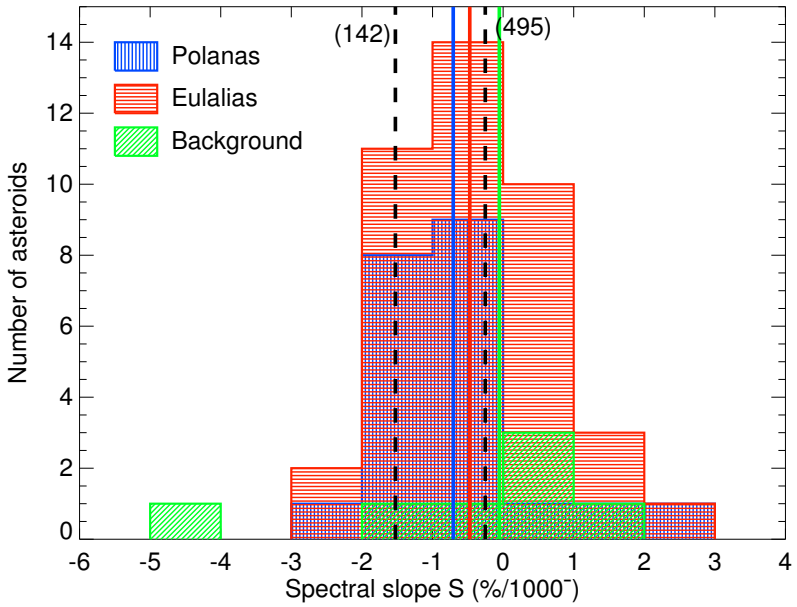

Figure 5: Distribution of the spectral slope S' for the asteroids of the Polana (blue) and Eulalia (red) families, and of the background population (green). The spectral slope has been computed between 0.55 and 0.90 μm. Colored vertical lines correspond to the mean slope of each group. Vertical dashed lines indicate the spectral slope of asteroids (142) Polana and (495) Eulalia.

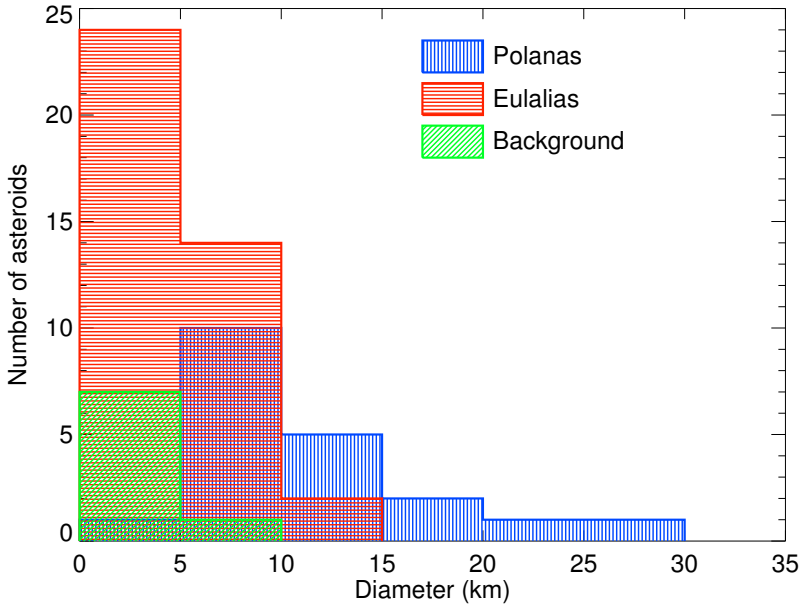

Figure 6: Distribution of the diameters for the asteroids of the Polana (blue) and Eulalia (red) families, and of the background population (green).

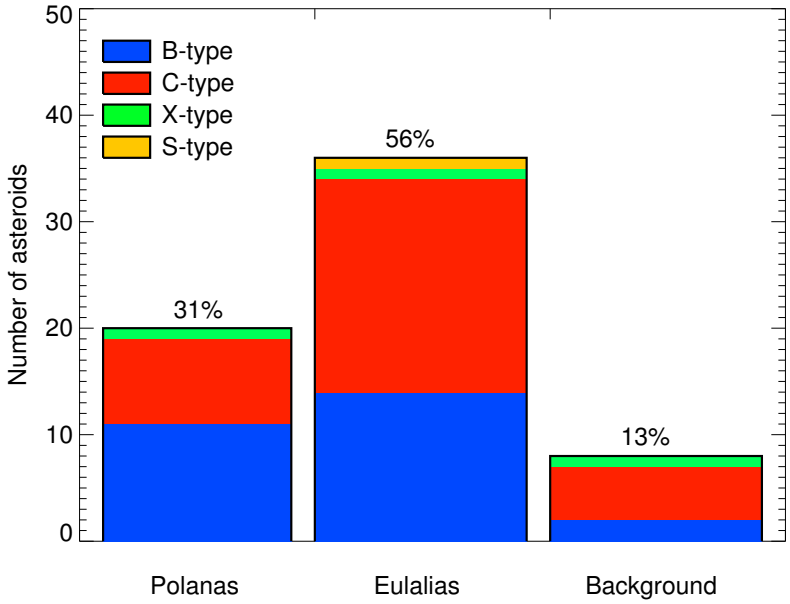

Figure 7: Statistical distribution of the asteroids presented in this work among the two colisional families, Polana and Eulalia, and the Background population. We show the percentages of asteroids that are members of any of these three groups. Shown within each group are the number of asteroids classified as B (blue), C (red), X (green), and S-types (yellow).

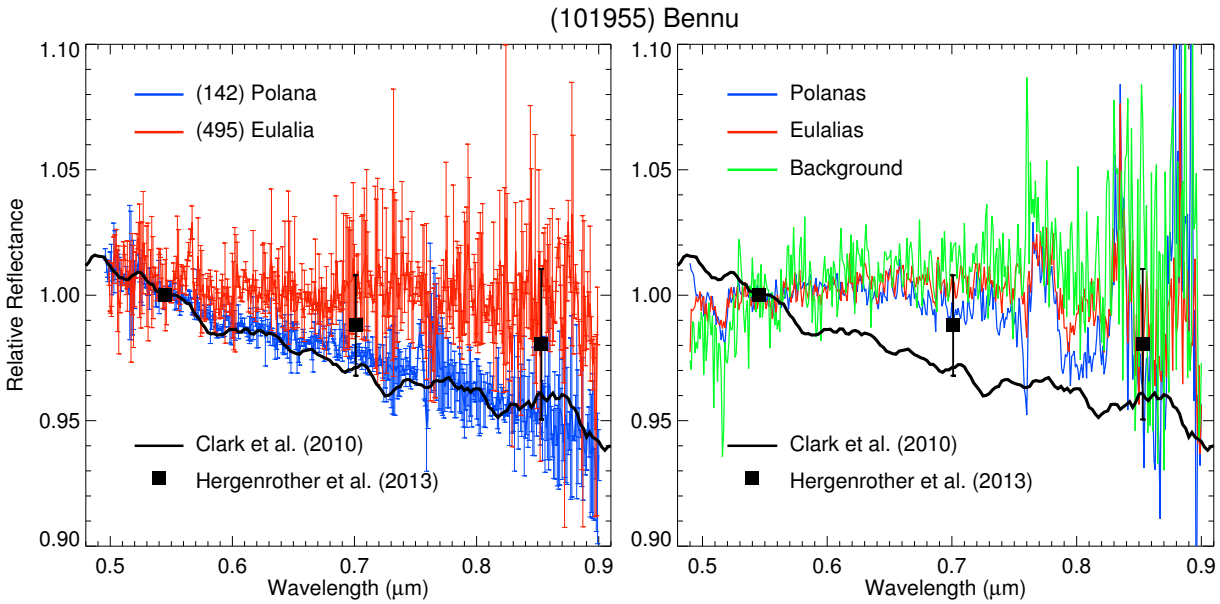

Figure 8: Visible spectrum (Clark et al., 2010) and ECAS photometry (Hergenrother et al., 2013) for asteroid (101955) Bennu, compared to the spectra of asteroids (142) Polana and (495) Eulalia (left panel), and to the mean spectra of the Polanas, Eulalias, and background population as computed in this work (right panel).

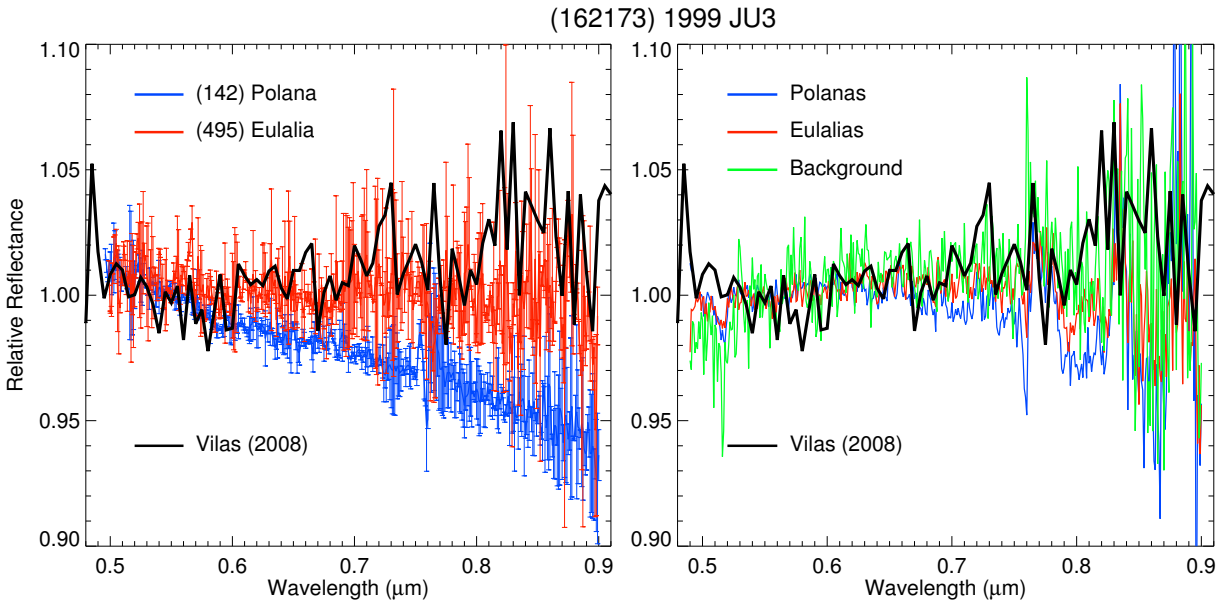

Figure 9: Visible spectrum from (Vilas, 2008) for asteroid (162173) 1999 JU_3, compared to the spectra of asteroids (142) Polana and (495) Eulalia (left panel), and to the mean spectra of the Polanas, Eulalias, and background population as computed in this work (right panel).

Appendix A. Individual spectra of the sample

Here we present the individual spectra of all the asteroids analyzed in this work. We include on each plot if the asteroids belongs to the Polana or the Eulalia families, or to the Background population, as well as the telescope used to obtain the spectra. The red lines correpond to linear fits between 0.55 and 0.90 μm, performed to computed the spectral slope S' in that wavelength range. All the spectra are normalized to unity at 0.55 μm.

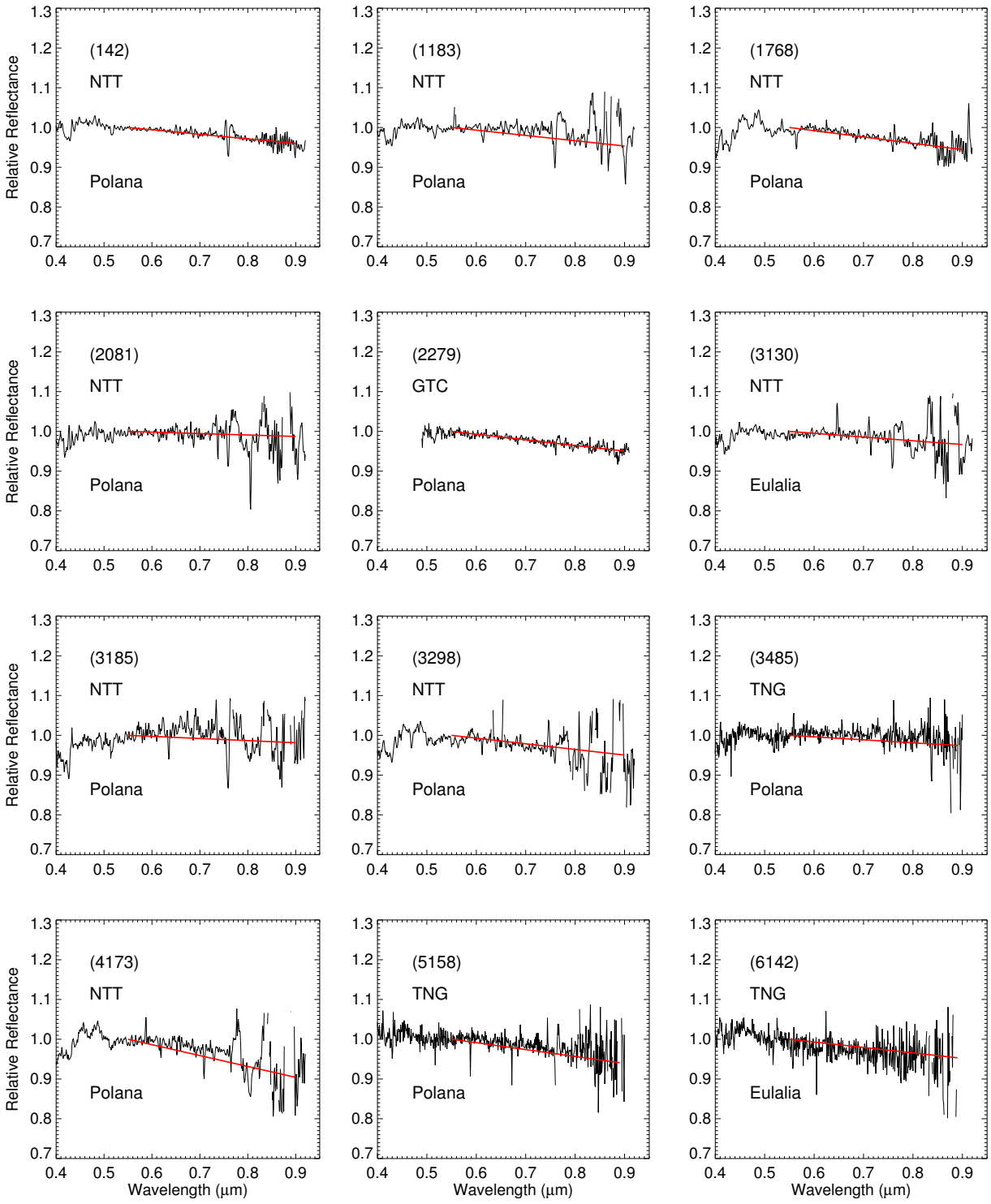

Figure A.10: Visible spectra of the asteroids analyzed in this paper. Linear fits (red) to the data points have been performed to compute spectral slope S' between 0.55 and 0.90 μm.

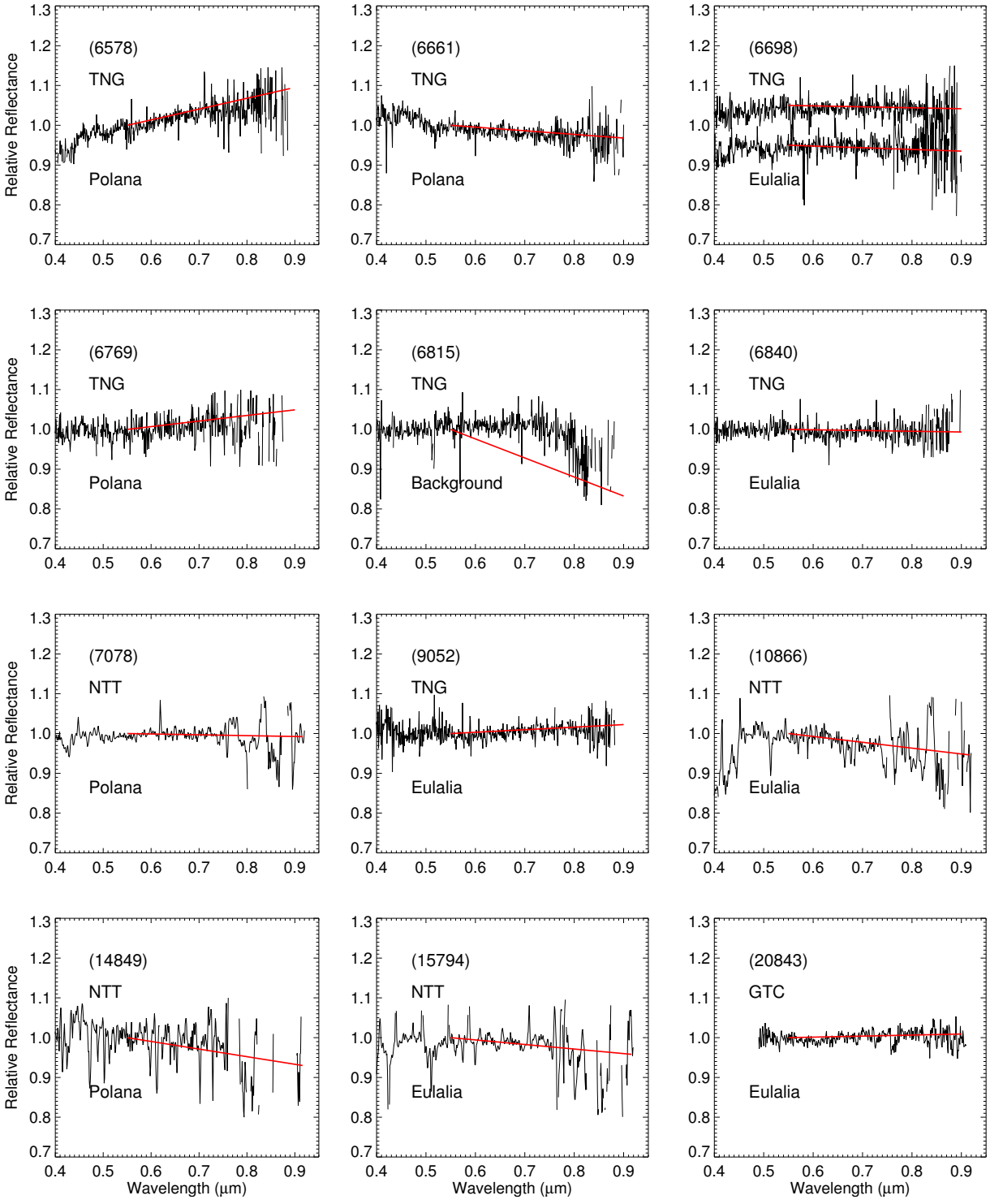

Figure A.10: (continued.)

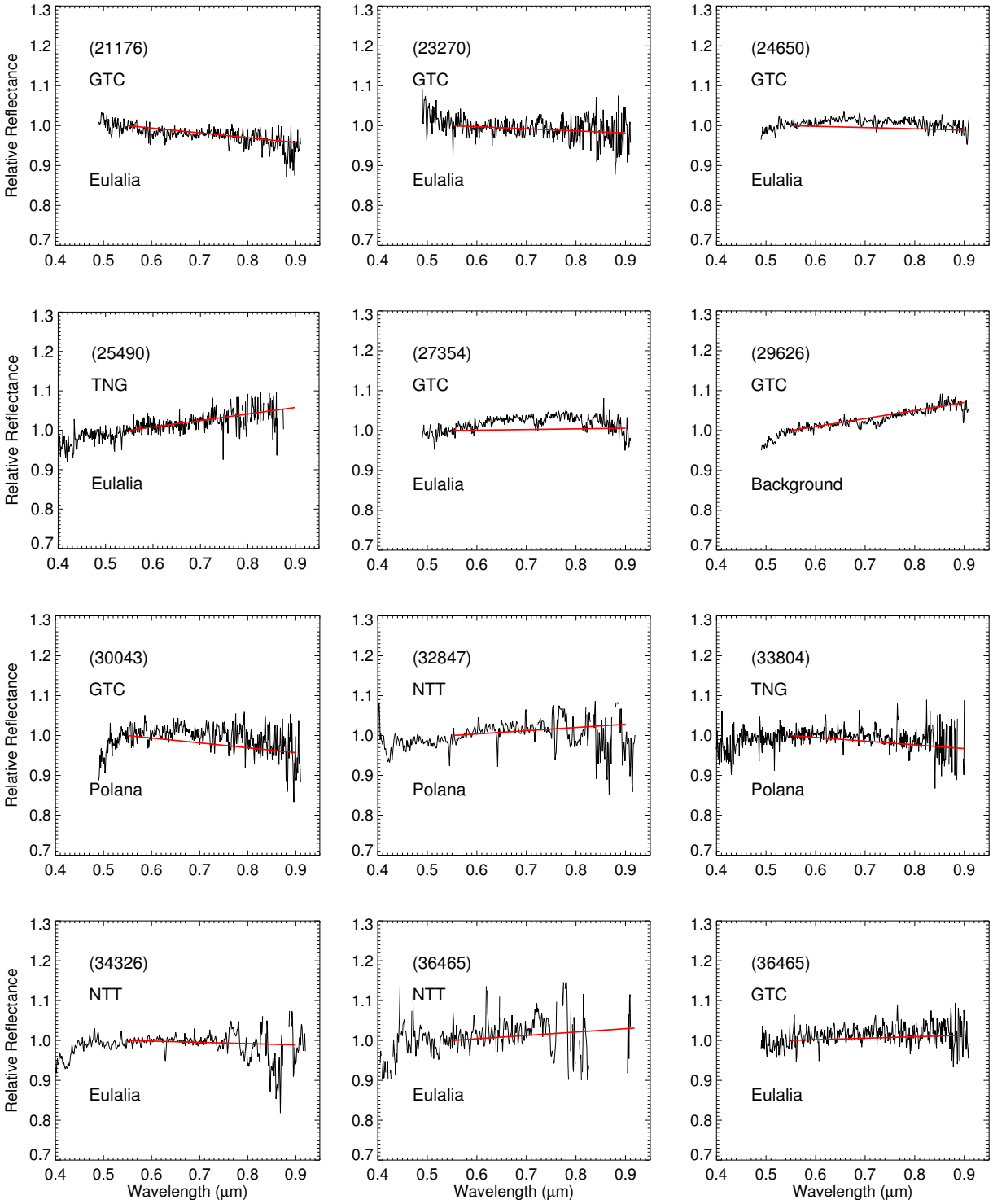

Figure A.10: (continued.)

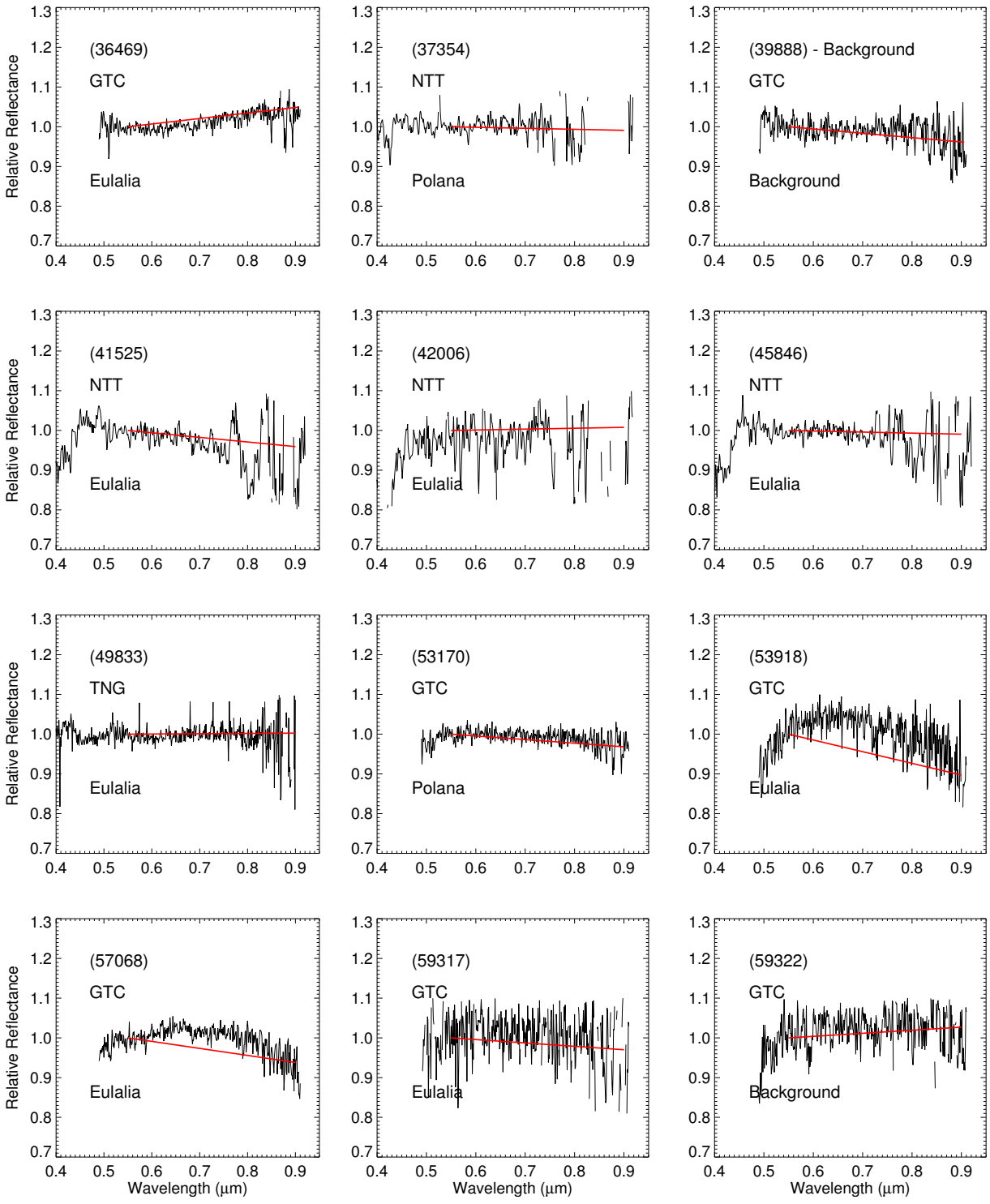

Figure A.10: (continued.)

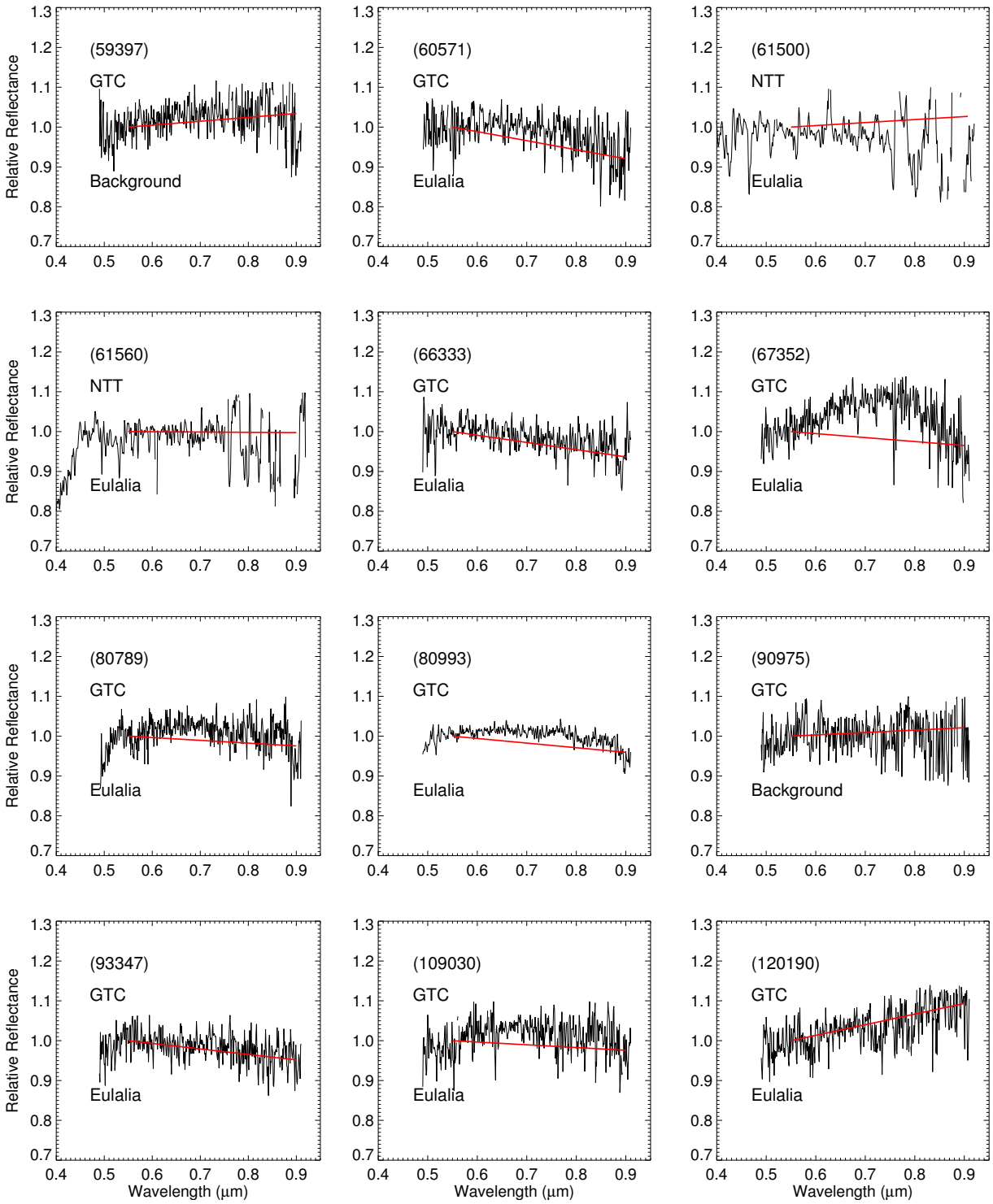

Figure A.10: (continued.)

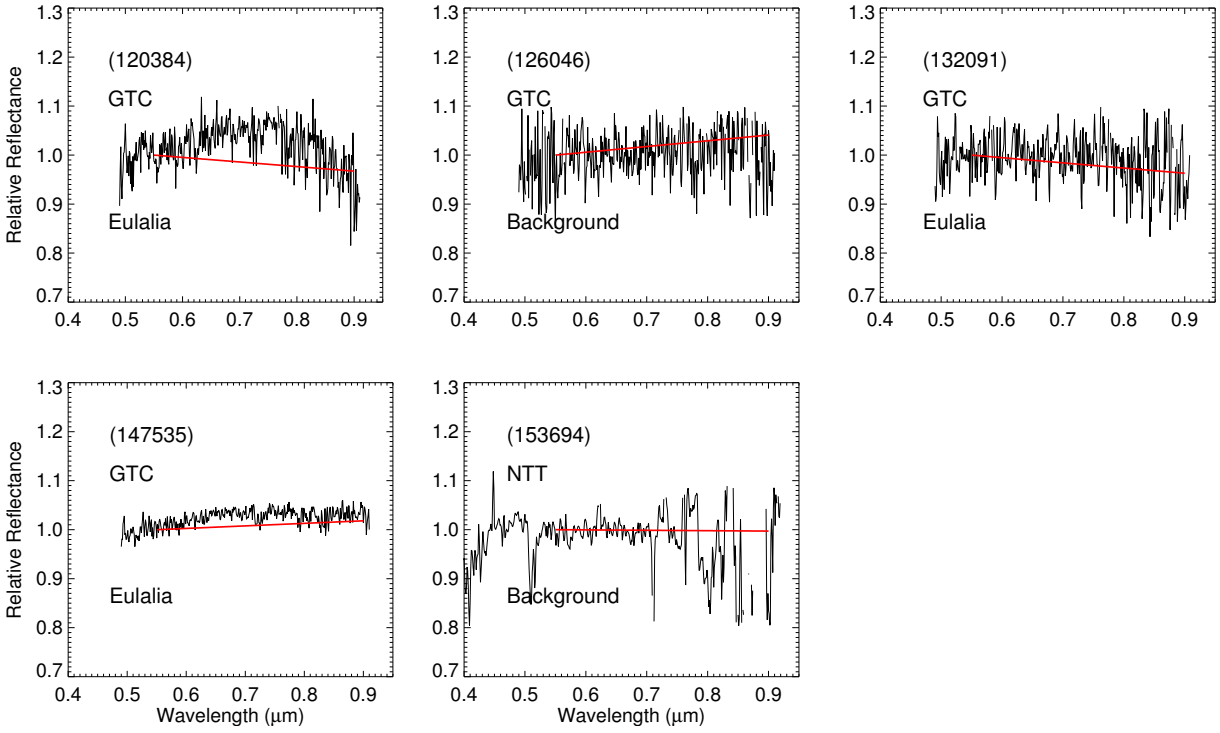

Figure A.10: (continued.)

References

Bottke, W. F., Jedicke, R., Petit, J., et al., 2002. Debiased Orbital and Absolute Magnitude Distribution of the Near-Earth Objects. Icarus, 156, 399-433

Bottke, W. F., Vokrouhlický, D., Walsh, K. J., et al., 2015. In search of the source of asteroid (101955) Bennu: Applications of the stochastic YORP model. Icarus, 247, 191-217

Binzel, R. P., Harris, A. W., Bus, S. J., et al., 2001. Spectral Properties of Near-Earth Objects: Palomar and IRTF Results for 48 Objects Including Spacecraft Targets (9969) Braille and (10302) 1989 ML. Icarus, 151, 139-149

Bus, S. J., & Binzel, R., 2002. Phase II of the Small Main-Belt Asteroid Spectroscopic Survey. A Feature-Based Taxonomy. Icarus. 158, 146-177

Campins, H., Morbidelli, A., Tsiganis, K., et al., 2010. The origin of asteroid 101955 (1999 RQ36). Astroph. J. Letters, 721, L53-L57

Campins, H., de León, J., Morbidelli, A., et al., 2013. The Origin of Asteroid 162173 (1999 JU_3). Astron. J., 146, 26-32

Cellino, A., Zappla, V., Doressoundiram, A., et al., 2001. The Puzzling Case of the Nysa-Polana Family. Icarus, 152, 225-237

Cepa, J., Aguiar, M., Escalera, V. G., et al., 2000. OSIRIS tunable imager and spectrograph. Proceedings of SPIE Conference Series. 4008, 623-631

Cepa, J., 2010. OSIRIS: Final Characterization and Scientific Capabilities. In: Diego, J. M. & Goicoechea, L. J. (Eds.), Highlights of Spanish Astrophysics V, pp 15

Clark, B. E., Binzel, R. P., Howell, E. S., et al., 2010. Asteroid (101955) 1999 RQ36: Spectroscopy from 0.4 to 2.4 μm and meteorite analogs. Icarus, 216, 482-475

de León, J., Campins, H., Tsiganis, K., et al., 2010. Origin of near-Earth asteroid Phaethon and the Geminids meteor shower. Astron. Astrophys. 513, 26-33

DeMeo, F., & Binzel, R. P., 2008. An extension of the Bus asteroid taxonomy into the near-infrared. Icarus, 202, 160-180

Dykhuis, M. J. & Greenberg, R., 2015. Collisional family structure within the Nysa-Polana complex. Icarus, 252, 199-211

Hergenrother, C. W., Nolan, M. C., Binzel, R. P., et al., 2013. Lightcurve, Color and Phase Function Photometry of the OSIRIS-REx Target Asteroid (101955) Bennu. Icarus, 226, 663-670

Johnson, T. V. & Fanale, F. P. 1973. Optical Properties of Carbonaceous Chondrites and Their Relationship to Asteroids. J. Geophys. Res. 78, 8507-8518

Ishiguro, M., Kuroda, D., Hasegawa, S., et al., 2014. Optical Properties of (162173) 1999 JU3: In Preparation for the JAXA Hayabusa 2 Sample Return Mission. Astrophys. J. 792, 74-83

Ivezić, Z., Lupton, R. H., Juric, M., et al., 2002. Color Confirmation of Asteroid Families. Astron. J., 124, 2943-2948

Landolt, A. U., 1992. UBVRI photometric standard stars in the magnitude range 11.5-16.0 around the celestial equator. Astron. J., 104, 340-371

Lauretta, D. S., Drake, M. J., Binzel, R. P., et al., 2010. Asteroid (101955) 1999 RQ36: Optimum Target for an Asteroid Sample Return Mission. Meteorit. Planet. Sci. Supp. 73, 5153

Lazzaro, D., Angeli, C. A., Carvano, J. M., et al., 2004. S^3OS^2: the visible spectroscopic survey of 820 asteroids. Icarus, 172, 179-220

Lazzaro, D., Barucci, M. A., Perna, D., et al., 2013. Rotational spectra of (162173) 1999 JU3, the target of the Hayabusa2 mission. Astron. Astrophys. 549, L2-L6

Luu, J. X. & Jewitt, D. C., 1990. Charged-coupled device spectra of asteroids. I. Near-Earth and 3:1 resonance asteroids. Astron. J., 99, 1985-2011

Mainzer, A., Bauer, J., Grav, T., et al., 2011. Preliminary results from NEOWISE: an enhancement to the Wide-Field Infrared Survey Explorer for Solar System Science. Astrophys. J., 731, 53-66

Milani, A., Cellino, A., Knežević, Z., et al., 2014. Asteroid families classification: Exploiting very large datasets. Icarus, 239, 46-73

Moskovitz, M. A., Abe, S., Pan, K-S., et al., 2013. Rotational characterization of Hayabusa II target Asteroid (162173) 1999 JU3. Icarus, 224, 24-31

Nesvorný, D. 2010. Nesvorny HCM Asteroid Families V1.0, EAR-A-VARGBDET-5-NESVORNYFAM-V1.0, NASA Planetary Data System

Nesvorný, D. 2012. Nesvorny HCM Asteroid Families V2.0, EAR-A-VARGBDET-5-NESVORNYFAM-V2.0, NASA Planetary Data System

Nesvorný, D., Broz, M., & Carruba, V. 2015. Identification and Dynamical Properties of Asteroid Families. To be published as a chapter in Asteroids IV. ArXiv e-prints arXiv:1502.01628

Parker, A., Ivezić, $\hat{Z}$., Jurić, M., et al., 2008. The size distributions of asteroid families in the SDSS Moving Object Catalog 4. Icarus. 198, 138-155

Pinilla-Alonso, N., de León, J., Campins, H., et al., 2015. Portrait of the Polana-Eulalia Family Complex: Surface homogeneity revealed from Near-Infrared Spectroscopy. Submitted to Icarus

Popescu, M., Birlan, M., & Nedelcu, D. A., 2012. Modeling of asteroid spectra - M4AST. Astron. Astrophys., 544, 130-140

Shepard, M. K., Clark, B. E., Nolan, M. C., et al., 2008. A radar survey of M- and X-class asteroids. Icarus, 195, 184-205

Sugita, S., Kuroda, D., Kameda, S., et al., 2013. Visible Spectroscopic Observations of Asteroid 162173 (1999 JU3) with the Gemini-S Telescope. 44th Lunar and Planetary Science Conference, 1719, 2591

Tholen, D. J. 1984. Asteroid taxonomy from cluster analysis of photometry. PhD. Thesis, Arizona University, Tucson, 166 pp.

Tsuda, Y., Yoshikawa, M., Abe, M., et al., 2013. System design of the Hayabusa 2 Asteroid sample return mission to 1999 JU3. Acta Astronautica 91, 356-362

Vilas, F., Smith, B. A., McFadden, L. A., et al., 2006. Vilas Asteroid Spectra V1.1, EAR-A-3-RDR-VILAS-ASTEROID-SPECTRA-V1.1, NASA Planetary Data System

Vilas, F. 2008. Spectral Characteristics of Hayabusa 2 Near-Earth Asteroid Targets 162173 1999 JU3 and 2001 QC34. Astron. J. 135, 1101-1105

Walsh, K., J., Delbó, M., Bottke, W. F., et al., 2013. Introducing the Eulalia and new Polana asteroid families: Re-assessing primitive asteroid families in the inner Main Belt. Icarus. 225, 283-297

Xu, S., Binzel, R. P., Burbine, T. H., and Bus, S. J. 1995. Small main-belt asteroid spectroscopic survey: Initial results. Icarus, 115, 1-35